Marine Pollution Bulletin
November 2020, Volume 160 Pages 111584 (14p.)
https://doi.org/10.1016/j.marpolbul.2020.111584
https://archimer.ifremer.fr/doc/00648/75982/

Characterization of south central Pacific Ocean wind regimes in present and future climate for pearl farming application

Dutheil Cyril [1, 2, *], Andrefouet S. [1], Jullien Swen [3], Le Gendre Romain [4], Aucan J. [1], Menkes C. [1]

[1] Institut de Recherche pour le Développement, UMR 9220 ENTROPIE (Institut de Recherche Pour le Développement, Université de la Réunion, Université de Nouvelle-Calédonie, Ifremer, Centre National de la Recherche Scientifique), BP A5, 98848 Nouméa cedex, New Caledonia
[2] IRD, LOCEAN (UMR 7159), BP A5, 98848 Nouméa cedex, New Caledonia
[3] IFREMER, Univ. Brest, CNRS, IRD, Laboratoire d'Océanographie Physique et Spatiale (LOPS), IUEM, Plouzané, France
[4] IFREMER, Unité de Recherche Lagons, Ecosystèmes et Aquaculture Durable, ENTROPIE (UMR 9220), BP 32078, 98897 Noumea Cedex, New Caledonia

* Corresponding author : Cyril Dutheil, email address : cyril.dutheil@io-warnemuende.de

Abstract :

In the South Pacific (SP) pearl farming atolls, wind is the main driver of lagoon water circulation, affecting dispersal and survival of pearl oyster larvae. To characterize typical wind conditions in the SP, wind regime classifications are performed from regional climate simulations using the WRF model, for present-day and for the end of the 21st century under RCP8.5 scenario conditions. At the daily time-scale, 4 regimes are identified: a trade-wind, a north-easterly, and two easterly regimes. Their characteristics are driven by large-scale circulation and climate modes of variability. In future projection, all regimes are characterized by a ~15% wind speed increase, while directions and occurrence frequencies undergo marginal changes. At the monthly time-scale that corresponds to pearl oyster pelagic larval duration, nine wind regimes are determined including three regimes with wind reversals. These regimes can be used to model typical lagoon conditions during larval dispersal.

Highlights

► Wind is one of the main drivers of atoll lagoon circulation and larval dispersal. ► Four wind regimes are identified at day-scale based on 10 m u-v wind components. ► 30-day long regimes characterize lagoon conditions during larval dispersal. ► Climate change could increase wind speed by 15% in the South Central Pacific.

Keywords : South Central Pacific atolls, Weather regime, Surface wind conditions, Pearl farming, Climate change

1. Introduction

The high islands and low-lying atolls of the Pacific Ocean host a large amount of biodiversity as well as several human production activities (e.g. fisheries, aquaculture, pearl farming) which are particularly affected by the natural variations of the atmospheric and oceanic conditions. Thus far, much work has been devoted to monitor and study the evolution of sea surface temperature (SST) and air temperature in tropical islands because these parameters are well measured by routine sensors and have a direct effect on the physiology of organisms. For instance, changes in biodiversity patterns, occurrences of coral bleaching and spread of marine diseases have been linked to SST variations (e.g. Harvell et al., 2002; Van Wynsberge et al., 2017a; Claar et al., 2018). In deep and shallow tropical lagoons, wind is one of the main drivers of water characteristics (temperature, residence time, plankton concentration, etc…), biological communities' processes (e.g., pearl oyster population spawning, Fournier et al., 2012) and physical circulation (Lowe and Falter, 2015; Thomas et al., 2011). In atolls with a high degree of aperture to the ocean, remote oceanic waves and tides may also have a strong influence (Lowe and Falter, 2015). Conversely, when atolls are closed or semi-closed by high elevation rims, their lagoons are then far less influenced by remote hydrodynamics (Dumas et al., 2012; Van Wynsberge et al., 2017b) and wind remains the main driver. On one hand, strong wind can generate local lagoon waves, whose effects on biological communities can range from beneficial to destructive. On the other hand, the absence of wind on several atolls during periods of days to weeks have led to dystrophic and massive mortality events primarily due to poor water renewal, stratification and anoxia (Andréfouët et al., 2015).

In a pearl farming context, especially in French Polynesia and Cook Islands, productive atolls are closed or semi-closed, and wind conditions are a determinant factor of the spat collection success and, henceforth, of the sustainability of the pearl farming activity (Andréfouët et al., 2012). Indeed, black-lipped pearl oyster, *Pinctada margaritifera,* larval growth and dispersal (Thomas et al., 2012, 2014, 2016) vary with wind, as the latter influences not only larvae movements but also the planktonic food dynamics. When these larvae are collected for mariculture purposes, wind conditions can partly explain differences between productive and unproductive locations and periods. The characterization of present-day and future wind regimes in French Polynesia and Cook Islands is thus a critical piece of information to understand the past and future rates of spat collections.

A method commonly used to characterize the regional wind conditions is a classification in weather regime (WR, e.g. Hopuare et al., 2019; Lefèvre et al., 2010). A WR can be defined as a large-scale atmospheric structure that appears recurrently in the study area, and induces recurrent local conditions. As they characterize robust yet simplified wind patterns, they have been used for example to study typical fish larval dispersion in the New Caledonian lagoon (Cuif et al., 2014). In addition, three recent studies (Hopuare et al., 2019; Lorrey and Fauchereau, 2018; Specq et al., 2019) have characterized regional WRs in the South Pacific, and studied how the large-scale signals of the Madden-Julian Oscillation (MJO) and El Niño Southern Oscillation (ENSO) modulate the frequency of occurrence of these WRs. These three studies each considered a different spatial domain, but none of them covered all of the atolls of French Polynesia and Cook Islands. In a pearl farming context, Thomas et al. (2014) used a classification method in WR to characterize the 1979-2011 wind conditions on the Ahe atoll in the North Tuamotu Archipelago of French Polynesia (Fig. 1a). They subsequently simulated different scenarios of larval dispersal and connectivity for *P. margaritifera*. However, no additional atoll has yet been studied to our knowledge.

The present study aims to investigate the WRs that affect all Polynesian central Pacific atolls at different spatial and temporal scales, with a focus on those hosting pearl farming activities (Fig. 1a), and to understand what may be their fate in future climate. Eventually, the assessment of the impact of wind patterns and changes on pearl farming activities requires a model of each lagoon hydrodynamics, which is beyond the scope of the present study (but see Dumas et al 2012, Thomas et al. 2016, and Le Gendre et al. this issue for selected atolls). Here, the scope is regional, and typical weather conditions and their climate variability (ENSO, climate change) are identified. This aims to improve our knowledge of the South Central Pacific wind regimes, and to provide the forcing conditions for future lagoon-dedicated hydrodynamic studies. Within this scope, pearl farming sets the time frame during which wind regimes are relevant. This time frame ranges from 1 day to 30 days. Weather can trigger spawning and control larval dispersal during a maximum pelagic larval duration (PLD) time, thus considered here to be 30 days, following Thomas et al. (2014) and Sangare et al. (2020).

In the present study, we use a methodology similar to Hopuare et al., (2019) and Specq et al., (2019) to calculate WRs, but we considered all the South-central Pacific, and projected the present-day WRs into future conditions. To that end, regional atmospheric simulations are performed with the Weather Research and Forecast (WRF) model for present day, and for the end of the 21st century under RCP.8.5 scenario. As climate models are known to have strong biases in the South Pacific region, bias correction methods are applied to reduce the uncertainties of simulations (Dutheil et al., 2019, 2020; Li et al., 2016). We first describe in section 2 the general features of the South Pacific climate and the state of the art of its future projections. The experimental design and the statistical methods for WR classification are described in section 3. In section 4, we describe and validate the present-day WRs at the daily scale, and discuss their projection in the future. The relation between WRs at the monthly and daily time- scale is given in section 5. Finally, in section 6 we discuss our results against previous studies, and highlight perspectives for lagoon modelling.

2. Background on the South Pacific climate

Large-scale weather and climate conditions in the South Pacific (SP) have been widely studied in recent decades (e.g. Brown 2020), and only their main features are summarized here. In the SP, the thermal balance between the equator and the subtropics combined with the Earth rotation produces an east-south-easterly mean flux (Fig. 1b). This large-scale circulation is modulated by the position and intensity of the South Pacific High located around Easter Island, and the low pressure system of the equatorial western Pacific (denoted by the white pressure contours and indicated by "H" and "L" respectively in Fig. 1b). The SP also exhibits the most intense convergence zone of the Southern Hemisphere named the South Pacific Convergence Zone (SPCZ). The SPCZ is a rainfall band diagonally-oriented (northwest to southeast, see pink contour in Fig. 1b), which stretches from Papua New Guinea to French Polynesia, and modulates the low-level circulation according to its position and intensity (e.g. Vincent, 1994; Brown et al., 2020). The SPCZ intensity and position are themselves modulated by many oscillations at different time scales such as seasons, El Niño-Southern Oscillation (ENSO), or the decadal oscillation (e.g. Vincent et al., 2011, Brown et al., 2020). For instance, during extreme El Niño events, the SPCZ undergoes an equatorward swing of up to ten degrees of latitude and collapses to a more zonally oriented structure (e.g. Cai et al., 2012; Vincent et al., 2011), conducting to very different weather conditions in the South central Pacific, such as an increase of potential of tropical cyclone genesis around French Polynesia (Vincent et al., 2011).

In addition to SPCZ variations, anthropogenic forcing is projected to modify the meridional thermal balance of the Earth with a heterogeneous global warming pattern. At the Pacific Ocean scale, the equator is expected to become warmer than the tropical South Pacific (e.g. Collins et al., 2010; Grose et al., 2014), inducing changes in the projected SP circulation and precipitation (e.g. Cai et al., 2012; Dutheil et al., 2019; Widlansky et al., 2013). Nevertheless, at the local scale, the SST warming pattern from the Coupled Model Intercomparison Project (CMIP) models remains uncertain, especially in southwestern Pacific. Indeed, Li et al. (2015, 2016) showed that the typical "cold tongue bias" found in the CMIP models is associated with insufficient mean precipitation and clouds over the western Pacific warm pool (Fig. 2a), which results in an underestimation of the convective feedback and an excessive SST warming response in the equatorial western Pacific. Li et al. (2016) then developed a statistical method to correct the SST bias, which is applied in this study and shortly explained in section 3.1. Previous works, that have studied the SPCZ changes under future climate scenarios using an SST bias-correction method, have shown a likely drying of the SPCZ with an increase of wind speed in the south central Pacific due to an increase of moisture divergence in response to the changes in SST (Dutheil et al., 2019, Widlansky et al., 2013). On top of these uncertainties on SST projections, the changes in SPCZ interannual variability need to be taken into account. Using a large set of global climate models, Cai et al., (2012) showed a possible strong increase (+81%) of "zonal SPCZ" events (*i.e.* shift of the eastern part of SPCZ towards the equator, which drastically modifies the large-scale circulation) due to anthropogenic forcing, although regional studies with atmospheric models did not reproduce these results (Chung and Power, 2016; Evans et al., 2016; Dutheil et al., 2019). In this study we used a regional dynamical framework that realistically simulates the SPCZ orientation and intensity in present-day conditions, and that projects a significant drying (-25%, see Fig. 6 in Dutheil et al., 2019 or here with the contours in Fig. 2bc) in the south central Pacific region associated to an increase of moisture divergence dominated by changes in large-scale circulation.

3. Material and Methods

3.1 Regional model configuration and experimental design

The atmospheric modeling framework used here is fully detailed in Dutheil et al., (2020). A brief summary is given here. We used the Weather Research and Forecasting (WRF) Model version 3.6.1 (Skamarock and Klemp, 2008) with a parent domain at 105 km resolution that encompasses the tropical Pacific region [101°E-59°W; 26°N-42°S]. A two-way nested domain over the South-West (SW) Pacific [145°E-130°W; 32°S-2°S] with an increased resolution of 21 km is included (see Fig. 1b). Both domains share the same 32 vertical levels.

A present-day (PD) simulation is first performed over the 1980-2016 period (37 years). Surface and lateral boundary conditions for the parent domain are prescribed from the 6-hourly outputs of the NCEP2 reanalysis (Kanamitsu et al., 2002).

To assess the WR response to anthropogenic forcing, we also perform a climate change (CC) simulation. This simulation is conducted by prescribing monthly anomalies for surface (SST) and lateral (wind velocity, air temperature, humidity and geopotential height) boundaries from the CMIP5 projections under the RCP8.5 scenario for the late twenty-first century. These future anomalies are computed as the difference between the 2080-2100 and 1989-2009 periods of multi-model mean monthly climatology from 31 CMIP5 models. This method is sometimes referred to as the pseudo-global warming (PGW) approach (Dutheil et al., 2019; Zhang et al., 2016). With this process, the synoptic and interannual variability at the boundaries keeps the same phase and amplitude as the PD simulation. In addition, as the SST warming pattern from the CMIP models remain uncertain especially in the SW Pacific with a typical "cold tongue bias", the SST projection bias is corrected according to Li et al. (2016) statistical method, named "emergent constraint" method. It consists in a correction of the SST anomaly projection based on the linear relationship between the historical precipitation bias and the SST warming in the equatorial western Pacific in CMIP5 models (Fig. 2b). This correction increase the meridional and zonal gradient of SST warming (Fig. 2cd), and allows to reduce the inter-model (CMIP5) spread in SST warming, and is supposed to improve the reliability of SST warming pattern projections. This strategy is fully explained in Li et al. (2016), and was applied by Dutheil et al. (2019, 2020) to assess changes in the SPCZ and SP tropical cyclone activity.

3.2 Identification of regional weather types by clustering

WRs are identified in a large domain around the targeted atolls [165°W-130°W;25°S-9°S] (blue box in Fig. 1b) using statistical classification methods. To that end, daily average of the 10-m zonal and meridional wind components (u,v), hereafter referred as surface winds, are computed from the WRF simulation for the 37 available years (from January 1980 to April 2016), thus including 13270 consecutive days. The data are first normalized and standardized using their mean and standard deviation computed over the 37-year period; then two classifications are performed: a first classification to extract the main WR patterns at the daily scale over the area of interest; and a second classification to determine typical 30-day sequences of weather events that can impact pearl oyster larvae growth and dispersal.

In order to extract the main modes of spatial variability of surface winds, we first perform a principal component analysis (PCA; Jolliffe, 2011) on the 13270 days of u and v data, each day of (u,v) being treated as an individual for the PCA. The twenty-first principal components are kept, representing 95% of the cumulative total variance. In that reduced space, the 13270 days are then classified using the k-means classification algorithm (Diday, 1971) to determine wind patterns (or regimes). This classification is referred hereafter as the ‘daily classification’.

A second type of classification is performed to analyze sequences of 30 consecutive days instead of individual days. The 30-day length corresponds to the generally agreed maximum PLD for *Pinctada margaritifera* (Thomas et al., 2011, 2014). As the average persistence of daily WRs is between 3 and 6 days (Fig. 5a), the 30-day sequences are separated by 10 days, similarly to Thomas et al. (2014). This ensures to avoid double counting an event, and to limit the gaps between sequences, which might miss events. The same type of classification described above is then performed. Each 30-day sequence of (u,v) maps is considered as an individual. First, a PCA is performed on the 1337 30-day sequences to identify the main modes of spatial variability. The 30 first principal components, representing 70% of the cumulative total variance, are then kept to perform the k-means classification. This second classification is named the “30-day classification”.

One of the limitations of the k-means clustering algorithms is that they require to define *a priori* the number of clusters (k), and many methods have been developed to determine the optimal number of clusters. The 'NbClust' function in factoextra R package allows comparing 26 of these methods, the reader could refer to Charrad et al., 2014 for a complete description of all these methods. The number of clusters kept in each approach (*i.e.* daily or 30-day classification) corresponds to the consensus between these 26 methods (Fig. 3).

Finally, to infer WRs in the future, two options are possible. First, the future WRs can be determined by projecting the future conditions on the present WR clusters, or the future WRs can be computed from future conditions, independently from present WRs, by clustering future conditions. The first option allows looking at how the future wind conditions may shift from a given prevailing regime to another, with respect to the present day conditions, but it will not show the future typical weather regimes unless one assumes that the regimes are stationary. This assumption is unlikely because an evolution of large-scale tropical fields is expected due to climate change (Dutheil et al., 2019; Gastineau et al., 2008; Tokinaga et al., 2012; Vecchi et al., 2006, 2008). Therefore, the second option is chosen, and future WRs are computed using surface winds from the CC simulation. However, in that case, it is not possible to track which of the present-day regimes transform into which of the future regimes. Nevertheless, future WRs can be compared with their closest present WRs. To do so, a distance matrix providing the distance between the centroid of each present and future WR is computed. The present and future clusters that have the minimum distance between them are paired, assuming that the closest future regime to a given PD regime tracks the regime evolution with climate change. The classification of future WRs is performed only for the daily WRs. Indeed, the ecological WRs (*i.e.* 30-day classification) are too variable in wind speed and direction to determine unambiguously an evolution from a present to a future regime, and the distance matrix indicates that several future regimes can be associated with the same PD regime. In the following, the WRs at daily scale will be noted “R”, and the WRs at 30-day scale will be noted “S” (for sequence).

3.3 ENSO modulation

As ENSO is the main mode of interannual variability in the SP, we characterize its influence on the occurrence of the WRs. To do so, we separate ENSO variations into 4 classes based on the ONI index (Oceanic Niño Index, https://origin.cpc.ncep.noaa.gov/products/analysis_monitoring/ensostuff/ONI_v5.php): La Niña ($ONI<-0.5$), neutral ($-0.5<ONI<0.5$), moderate El Niño ($0.5<ONI<1.5$), and extreme El Niño ($ONI>1.5$) conditions. Extreme El Niño events are characterized by a 10° northward shift of the SPCZ, the wind anomalies are stronger and move eastward relative to moderate El Niño events. It is therefore likely that the probabilities of occurrence of each WR will be different for these two El Niño modes. For each WR, the occurring days are distributed over the 4 phases of ENSO to derive the observed WR distribution per ENSO class (O: number of days of regime occurrence for each ENSO phase). The expected distribution (E) for each phase is computed assuming that the distribution of regimes does not depend on ENSO, it is thus equal to the total WR distribution weighted by the number of days of each phase. We then use a Chi-square test as in Lefèvre et al. (2010) to evaluate if the null hypothesis is verified, *i.e.*, if O is equal to the expected distribution E and thus the distribution of regimes would not depend on ENSO, or not.

$$\chi^2 = \sum_{1:4} \frac{(O-E)^2}{E}$$

The probability that a random distribution provides a value larger than χ^2 is given by the χ^2 p-value. In our analysis, neutral ENSO conditions are included, implying a Chi-square test with 3 degree of freedom. The χ^2 goodness-of-fit does not indicate which phases are significant. This is done by the standardized residual $R = (O-E)/(E)^{1/2}$, which determines which phases are major contributors when the null hypothesis has been rejected. When *R* has a magnitude greater than 2.0, the corresponding ENSO phase significantly influence the occurrence frequency of WR (Lefèvre et al., 2010; Leroy, 2006; Specq et al., 2019).

3.4 Observations datasets

To illustrate the mean climate conditions in the Pacific we use the Climate prediction center

M
e
r
g
e

4. Results: Daily WRs

4.1 Climatological features in present-day

Four WRs are identified using the k-means clustering algorithm (Fig. 4, Table 1). The first WR is a trade wind regime with a strong homogeneous east-south-east flow (Table 1, Fig. 4e). It is the most frequent, occurring ~30% of the time (Table 1), with a seasonal predominance in austral winter (Fig. 5b). R2 and R3 are two easterly regimes (Fig. 4fg), which are also quite frequent (25-30% of the time, Table 1), but have different seasonal variations and persistence (Fig. 5ab). R2 occurs all year long and is the less persistent (Fig. 5a), lasting more than 3 days in only 40 % of its occurrences, while R3 is more frequent in austral summer (Fig. 5b), and is the most persistent, lasting more than 3 days in more than 50%, and more that 6 days in 20% of its occurrences (Fig. 5a). R4 is a north-easterly flow (Fig. 4h), which mainly occurs during austral summer and almost disappears during winter (Fig. 5b), and is the least frequent of the WRs (Table 1).

A
n
a
l
y
s
i
s
o
f

P
r

In general, WRs computed from ERA5 and WRF PD winds are in good agreement (Fig. 4abcd vs 4efgh; Table 1), with similar pattern, magnitude and occurrence, even if the PD simulation shows slightly stronger gradients than ERA5 with stronger strong winds and weaker weak winds (~±0.2m.s^{-1}). This could be associated to some biases in WRF but also to a slightly increased effective resolution in WRF compared with ERA5 allowing the resolution of stronger gradients. Overall, the favorable comparison underlines the ability of our model to realistically represent WRs in this region.

To understand the synoptic-scale context in which each WR occurs, composites of atmospheric conditions (*i.e.* sea-level pressure, surface wind and rainfall) for each daily WR over a larger domain [160°E-90°W;40°S-5°N] are displayed in Figure 6. R1, the trade wind WR, is mainly associated with an intense high pressure system located in the south of Tahiti commonly called Kermadec High (identified by the "K" letter in Fig. 6), and a low pressure system in the southwest equatorial Pacific. This situation mainly occurs in austral winter (Fig. 5b), when the SPCZ is contracted toward the west and the equator (pink line in Fig 5a), and when the Kermadec High is located eastward (around 140°W) to its usual location (near Kermadec islands as in Fig. 6d). This position of the Kermadec High (*i.e.* south of Tahiti) combined with the strong intensity of the equatorial low pressure zone explains the tightened isobars in the central South Pacific and the strong south-easterly flux (Table 1).

R2 is driven by two intense high pressure systems, the Kermadec High (K) centered at 160°W and the South Pacific High (identified by the "SP" letter in Fig. 6) to the east of our domain (Fig. 6b). The SP High causes an easterly flow which occurs in the east of the domain. The Kermadec High is located further west than in R1, producing a south-easterly flow that occurs in the southwestern part of the WR domain (blue box in Fig. 6b).

R3 is an easterly flow mainly driven by the SP High centered to the east of 90°W (Fig. 6c). This WR occurs mainly in austral summer (Fig. 5b), when the Kermadec High is replaced by the Tasman High pressure system in the Tasman Sea west of New Zealand (identified by "T" letter in Fig. 6c). The easterly flow is deviated southward west of 150°W, tilting the isobars to the South, due to the gap between the South Pacific High and the Tasman High pressure systems. The decrease of wind speed from east to west is associated to the untightened isobars in the west of the WR domain.

Finally, R4 is driven by the Kermadec High and the South Pacific High (Fig. 6d). The South Pacific High is located further north than the Kermadec High, which produces a strong tilt of the isobars in the gap between these two systems between 130°W and 150°W. West of 150°W, the isobars straighten up and the wind direction is south-east.

The spatial heterogeneity of each regime produces contrasting conditions between atolls in the region, but also within the same archipelago. For instance, for R2, wind speeds are higher in the Cook Islands than in the west and then the east Tuamotu Archipelago, but it is the opposite for R3

(Fig. 4fg). Similar conclusions can be made about wind direction. Therefore, independently of other parameters that may influence the circulation in the lagoon, the same WR may have different impacts on the circulation of lagoons in two different archipelagos or even within the same archipelago.

4.2 Interannual variability: ENSO modulation

The tropical Pacific SST pattern is modulated by large-scale climate modes at different timescales, such as ENSO at inter-annual scale (Timmermann et al., 2018), or the Interdecadal Pacific Oscillation (Salinger et al., 2001) at decadal timescales. In this subsection we explore and characterize the influence of ENSO modes on the occurrences of each WR.

The results of the Chi-square test (Table 2) suggest that all WRs are significantly influenced by ENSO. The extreme El Niño phase is the only ENSO mode that significantly influences the occurrence of all WRs, with R2 and R4 being more frequent and R1 and R3 conversely less frequent. Despite the radical behavior of the extreme El Niño phase (Fig. 7e), it is the moderate El Niño phase that has the strongest influence on R1. The neutral phase has almost no influence on R1, R2 and R3, while it negatively influences R4 (*i.e.* less occurrences). Finally, La Niña phase has an opposite influence on the occurrences of each WRs compared to El Niño phases.

As expected, ENSO influences the frequency of occurrence of the WRs and their anomalies. We compared the anomaly of each WR (difference between the WR pattern and the whole simulation average pattern) and the ENSO anomaly pattern (difference between ENSO phase and the whole simulation average pattern). The anomalies (Fig. 7) are similar when the given ENSO mode has a positive influence on regimes (i.e., increase in the WR frequency of occurrence). For instance, R2 is positively influenced by extreme El Niño phases (R=6.3 in Table 2), and the wind anomalies in R2 (Fig. 7b) are consistent with the wind anomalies during extreme El Niño events (Fig 6e), with a similar dipole in both cases (spatial correlation of 0.88, Table 3). Furthermore, R4 is positively influenced by moderate El Niño phase (R=3.9 in Table 2). The wind anomalies in R4 (Fig. 7d) are negative on almost the entire domain with a minimum in the northwest corner, and a similar wind anomaly pattern is representative of the moderate El Niño events (spatial correlation of 0.80, Table 3).

Between pearl farming atolls in the studied regions, ENSO influences differently the wind regimes, contributing to a further differentiation of their environment at decadal scale. As explained in section 2, during extreme El Niño events the SPCZ is moved of 10° northward, resulting in an increase of moisture transport convergence at the equator and a decrease in the South Central Pacific. Therefore, extreme El Niño events tend to increase the wind speed in Cook and Society Islands and decrease in Tuamotu (Fig. 7e). Conversely, during moderate El Niño events the SPCZ moves less northward (compared to extreme events) and the eastern part of the SPCZ is almost unaffected.

Therefore, the decrease of moisture transport convergence occurs further west and has no impact on the South Central Pacific. Thus, equatorial east wind anomalies can propagate further south, and wind speed is reduced for almost all atolls in the South Central Pacific. Finally, during La Niña events, the SPCZ moves southward, resulting in an increase of the moisture transport convergence in the South Central Pacific associated with north-east wind anomalies and very slight increase of speed.

4.3 Daily WRs in future conditions

In general, future WRs are similar to the present WRs, with marginal changes in their main characteristics (Fig. 4). All WRs in future conditions exhibits stronger wind speed and slight changes in wind direction and frequency of occurrence (Table 1).

The large-scale changes for R1 show strong positive pressure anomalies in the southern part of the domain centered on the Kermadec High, while in the northern part of the domain the positive pressure anomalies are weaker (Fig. 6i). These surface pressure anomalies result in an increase in the surface pressure gradient that generates stronger wind over the entire domain (+0.8m.s^{-1}; Fig. 4eim and Table 1). The highest surface pressure anomalies are also associated with negative precipitation anomalies (i.e. drying).

For R2, the wind speed increases all over the domain except in the south-east corner (Fig. 4fjn). These changes are associated to a surface pressure increase of the South Pacific High and the Kermadec High which dries the entire domain south of 10°S except for a small plume-shaped area between 140°W and 110°W (Fig. 6bfj). This wetter region coincides with the area of reduced wind speed (Fig. 6j). In addition, this regime becomes less frequent in future conditions, with a relative decrease of ~18%.

For R3, strong off-center surface pressure anomalies at about 30°E from the center of the South Pacific High occur in the southwest. The surface pressure anomalies display a south-north gradient (Fig. 6k) that increases the absolute surface pressure gradient (Fig. 6g) and the wind speed (Fig. 4gko) in the CC simulation. These changes also slightly alter the wind direction (+6.6°N), and the frequency of occurrence is 11% higher relative to present conditions.

Finally, for R4, the wind direction is shifted by +12°N, while the wind speed (+0.4 m.s^{-1}) and frequency of occurrence (+6%) experience minor changes (Fig. 4hlp and Table 1). In the north-east part of the domain, wind speed increases (~+0.6 m.s^{-1}) and wind direction of anomalies are south-east, while in the south-west part of the domain the wind speed decreases (-0.4 m.s^{-1}) and the wind direction of anomalies turn north-west (Fig. 6dhl). These changes are associated with an intensification of both SP and T high pressure systems (Fig. 6dhl). The increase in surface pressure is accompanied by a gradient of south-north and east-west surface pressure anomalies, which strengthens wind speed in the entire domain south of 10°S, except in the area between both high pressure systems. In this area, the space between the isobars is large, wind speed decreases (Fig. 4p), and precipitation increases (Fig. 6l).

The general picture is that, in future conditions, the high pressure systems located south of the domain tend to intensify (contours in Fig. 6ijkl) inducing a stronger south-north surface pressure gradient which generates stronger winds (Fig. 4mnop). Small areas of lower wind speeds appear concurrently with increased precipitation in regions of heavy rainfall (see pink lines in Fig. 6, Fig. 4mnop vs. 6ijkl), where the convergence of surface moisture increases mainly due to an increase in wind convergence (not shown). Globally, the consequences of CC would be stronger and more southerly winds for R1, R2 and R3 in all atolls of South Central Pacific expect Gambier archipelago where it is predicted a decrease of wind speed for R2. For R4, the wind speed decreases in all the archipelagos except in the north of Tuamotu where there are virtually no changes.

5. Results: 30-day regimes

5.1 General description

The 30-day classification leads to nine WRs. To discuss and summarize these nine 30-day WRs, a typology based on the variations of wind direction is designed and the synthesis is displayed in Table 4. Discriminating WRs based on the variation of wind direction is justified as regimes experiencing shifts in directions should generate more complex larval dispersal trajectories (Thomas et al., 2014).

The S3, S4, S6, S7, S8 and S9 regimes exhibit a steady east direction throughout the 30-day sequence with minor variations in their directions (Fig. 8b). The difference between each of these regimes is mainly due to wind speed (Fig. 8a). S3 (brown line, Fig. 8a) is the most intense, with a steady wind speed exceeding 6 $m.s^{-1}$ throughout the 30-day sequence. S4 (blue line, Fig. 8a) exhibits an intense wind speed during the first 15 days (~5.7 $m.s^{-1}$), then it decreases to ~3.8 $m.s^{-1}$. S6 and S7 (red and black lines in Fig. 8) are relatively steady throughout the 30-day sequence (~4.5 $m.s^{-1}$) with some weak variations (+-0.5 $m.s^{-1}$) which are in opposition of phase between S6 and S7. In S8 (light blue line, Fig. 8a), the wind speed is moderate at the start (~4 $m.s^{-1}$) then it increases until the 22nd day and stabilizes afterward around 6.2 $m.s^{-1}$. S9 (yellow line, Fig. 8a) is the least intense of the six regimes (~3.3 $m.s^{-1}$ in average), and its wind speed varies little. All these regimes occur almost 10% of the time each, except S6 (red), which is the most frequent (~15% of the time).

By contrast, S1, S2 and S5 exhibit significant changes in wind direction throughout the 30-day sequence (see Fig. 8d and Table 4). For S1, the wind direction is first oriented from the east, then at day 10, it deviates from north-eastward (grey line, Fig. 8d). In parallel, wind speed decreases from

4.7 m.s^{-1} to 3.0 m.s^{-1} (Fig. 8c). This regime is the second most frequent regime (more than 14% of the time) after S6. For S2 (purple line, Fig 7cd), the wind direction deviates gradually from east-north-east to north-north-east until day 15, and then gradually comes back to east-north-east at the end of the 30-day sequence, while the wind speed slightly decreases along the 30-day period (from 3.7 to 2.7 m.s^{-1}). This regime is the least frequent (6.2% of the time). Finally, S5 (green line, Fig. 8d) exhibits first winds from the north-east which eventually shift eastward. In parallel, wind speed is initially weak (>3.0 m.s^{-1}), and rises up to 4.5m.s^{-1} at the end of the 30-day sequence (Fig. 8c).

5.2. Relationships between the 30-day and the daily regimes

In the previous section, the spatial average of the 30-day WRs have been computed to characterize the temporal evolution of these regimes. In order to describe their regional pattern, and their relation to the daily WRs, the 30-day sequences are split into five 6-day sequences, and each of the 6-day sequence is associated to a daily WR. The pattern evolution of the direction-changing 30-day WRs (S1, S2, and S5) is presented in Figure 9.

S1 starts with a moderate easterly wind over the whole domain as in R2 (Fig. 9a vs 4f). Then, in the western part of the domain, the wind direction is deviated from east to north-east, similarly to R3 (Fig. 9c vs 4g). At the end of the 30-day sequence, the wind direction is north-east in almost all of the domain, except in the south-western part where the wind direction is south-east, similarly to R4 (Fig. 9e vs 4h). For S2, the spatial pattern of wind is first quite similar to R3, with an east flux in the east part of domain and a north-east flux in the western part of domain, and the wind speed decreases gradually from north-east to south-west (Fig. 9f vs 4g). Then the wind direction is deviated to north-east, and the wind speed decreases, like in R4 (Fig. 9h vs 4h). At the end of the 30-day sequence, the pattern seems to return to its initial state, *i.e.* in R3 configuration (Fig. 9j vs 4g), with a wind direction mostly easterly, except in the western part where the orientation is always northeast. S5 exhibits first a spatial pattern similar to R4 with a north-east flux (Fig. 9k vs 4h). Then the wind speed increases and the wind is gently deviated from north-east to east, with a spatial pattern similar to R3 (Fig. 9m vs 4g). Then the wind continues to increase, and the direction clearly stabilizes east at the end of the 30-day sequence, thus resembling to R1 (Fig. 9o vs 4e).

Overall, the patterns of the 30-day WRs time slices can be seen as a succession of daily WRs, even if the latters show smoother patterns in Figure 4 due to the large averaging (numerous days are averaged in Figure 4, while Figure 9 shows the evolution of the barycenter of each of the 30-day WRs). To summarize, S1, S2 and S5 can be seen as a succession of daily WRs:

S1: R2 → R3 → R4

S2: R3 → R4 → R3

S5: R4 → R3 → R1

5.3. Regimes for selected atolls

As illustrated in Figures 4 and 9, the WR patterns show a quite large regional variability in terms of wind speed and direction which will affect the different sub-regions of interest (Fig. 1a).

Therefore, we aim to emphasize here that despite the low distance between the atolls, certain regimes can have very different characteristics some regimes may have very different characteristics from one regime to another. Although more computations and comparison can be done to reinforce this idea, we first characterize the wind conditions for specific pearl farming sites of the south central Pacific region, especially focusing on the three 30-day WRs with wind changing directions. To that end, we selected six sites considering their history of scientific research (Fig. 1a): namely Ahe, Raroia and Hao atolls in the Tuamotu archipelago, Mangareva which is the main Gambier island, and Aitutaki and Manihiki in the Cook Islands, and we extracted their 30-day WRs (Fig. 10).

Regarding the wind direction, for the three 30-day WRs, the three Tuamotu atolls show a very similar 30-day pattern, with only Hao exhibiting slightly more pronounced NNE and NE direction shifts when the wind direction is lower than 60°. Interestingly, its slightly southern location (compared to Raroia) has a certain influence on its characteristic 30-day WRs. Mangareva, which is at the most south-eastern part of the domain shows the largest wind direction variations for the three 30-day WRs. Manihiki and Aitutaki are located on the western part of the domain but at a very different zonal position. Consequently, they exhibit quite different wind directions, Manihiki in the north exhibiting a temporal evolution close to the Tuamotu atolls while Aitutaki in the south showing abrupt changes in wind direction particularly for S2.

6. Discussion

6.1. Regional daily WRs

In this study we characterized the weather regimes in the south central Pacific region at different temporal scales (i.e. daily and 30-day scales), in present and future conditions. The weather regimes are identified from two regional simulations (*i.e.* in present-day and climate change conditions) performed with the WRF model in a nested configuration at 21 km resolution. The climate change simulation is performed under the RCP.8.5 scenario for the end of the 21st century. We used a PGW approach and an emergent constraint method to correct at the same time historical and projected

SST biases in order to reduce the uncertainties of the climate simulations. Then, two types of classification by weather regimes are performed from simulated surface winds, at the daily and 30-day scales. The “daily classification” revealed four weather regimes: a strong trade wind, two easterly flows, and a north-easterly flow. A similar classification from ERA-5 reanalysis shows a very good agreement with the weather regimes identified from the PD simulation.

Two recent studies (Hopuare et al., 2019; Lorrey et Fauchereau 2018) also performed a weather classification in the South Pacific, but over different periods (1979-2015 and 1950-2014, respectively) and domain extents ([205.5°E-215.25°E;12°S-22.5°S] and [160°E-230°E;30°S-10°N], respectively) and from different data sets (surface wind from NCEP2 reanalysis and geopotential heights from NCEP/NCAR1, respectively). Despite a different domain size between Hopuare et al (2019) and this study, the four weather regimes identified in Hopuare et al., (2019) are very close to ours, a likely explanation is that the two domain centers are almost co-located (*i.e.* near to Tahiti). By contrast, six WRs were found in Lorrey et Fauchereau (2018) instead of four in Hopuare et al., (2019) and the present study. This difference can be likely explained by the domain extent that encompasses a wider region and the domain center which is much further west and north than ours, thus capturing weather conditions and synoptic structures that are not included here as the north-west Pacific monsoon or Tasman high.

6.2. Influence of climate modes of variability and future projections

The regimes identified here are mainly controlled by the position and intensity of synoptic structures (e.g. western equatorial low, Kermadec High etc…) themselves modulated by the season and ENSO mode. Indeed, the occurrence of the four WRs is modified by the ENSO mode, and the strongest influence occurs during extreme El Niño events.

In future climate, the projections show an intensification of these regimes, with a 15% increase in wind speed mainly explained by an intensification of meridional pressure gradient in response to SST changes. The strength of our framework, thanks to an emergent constraint method (Li et al., 2016) and a PGW approach, is to correct for the known SST biases in CMIP models (such as double ITCZ or cold tongue biases) which limit the confidence that can be given to climate projections in the South Pacific (e.g. Brown et al., 2020). The impact of the emergent constraint method has been evaluated by comparing with an experiment without correction. This experiment revealed significant consequences for R4, in particular a more intense drying in the northwest and a stronger decrease in wind speed in the southeast in the corrected simulation compared to the uncorrected one (not shown). The main limitation of this correction is the assumption of a linear relationship between the present-day precipitation and the projected SST pattern in CMIP5 models in the western equatorial Pacific (Fig. 2b), which is not perfect (r=-0.57).

The PGW approach has also some shortcomings. Namely, it does not allow assessing the influence of a change in ENSO variability, since the inter-annual variability in SST is kept constant in the climate-change simulation compared to the present-day simulation, because only monthly climatology anomalies are added. However, recent studies predicted an increase of extreme El Niño events frequency in warming climate (e.g. Cai et al., 2012, 2014, 2018), with especially an increase of 81% of SPCZ zonal events for the end of the 21st century in the RCP8.5 scenario (Cai et al., 2012). Therefore, it is likely that these changes in ENSO variability will alter the frequency of occurrence of the weather regimes that have been determined here. Under present conditions, extreme El Niño events increase the frequency of R2 and R4 and inversely for R1 and R3, therefore if we consider this process and if we follow the results of Cai et al. (2012), it is likely that this trend will add to the trend due to the mean climate change alone. Thus, this trend due to change in inter-annual variability could increase or decrease (according to the WR considered) the frequency changes found in this study. Furthermore, R2 and R4 being the most spatially contrasting regimes, changes in inter-annual variability could accentuate the differences in wind conditions between the eastern and western atolls of the SCP.

6.3. WRs and their relevance to pearl farming

The main purpose of this study was to provide information on the wind conditions that prevail on pearl farming atolls across a vast Pacific Ocean domain, at different time scales. In addition to the daily-scale, a maximum PLD time considered here was 30 days. Thomas et al. (2014) also performed a “30-day classification” but only on Ahe atoll in the western Tuamotu and using ERA-Interim wind surface over the 1979-2011 period, to characterize periods of pearl oyster larval dispersal. They identified twelve 30-day wind regimes with average characteristics quasi-similar to those determined here (wind speed between 3.7 and 7.6 $m.s^{-1}$ and wind direction between 76°N and 100°N). However, Thomas et al. (2014) did not identify 30-day regimes with a changing wind direction contrast to the present regional-scale study. The synoptic scale of our work allows demonstrating that, even with a limited-number of wind regimes, the different atolls are exposed to significant weather variations across the domain. This variability has important consequences for pearl farming.

Knowledge of wind regimes opens fresh perspectives to create new products relevant for pearl farming management. First, lagoon hydrodynamics and connectivity modeling studies (Dumas et al., 2012; Thomas et al., 2012, 2014, 2016) can help understanding sink areas for *Pinctada margaritifera* larvae and therefore the most suitable areas for spat collection. For this application, hydrodynamic modeling of atoll lagoons requires high resolution dedicated model for each location, including a good representation of the local geomorphology, and the influence of other forcing factors such as waves and tides (Le Gendre et al. this issue), but wind remains a key component. These 'sink' areas should have good potential for spat collecting (although we point out that actual recruitment and survival of the spats is not guaranteed). In this context, atoll hydrodynamic models can be run for different types of regimes in order to understand the distribution of the sink areas according to a range of recurrent wind conditions. It is recommended to customize the analysis for atolls located far apart, since we observed difference between six specific atolls and islands distributed far apart (Manihiki, Aitutaki, Ahe, Raroia, Hao and Mangareva). Weighting the results by the frequency of the local regimes (Fig. 8) can provide a way to identify what would be, statistically speaking, suitable areas for the activity for a typical year. This information can further be used for the spatial planning of concessions. Indeed, the French Polynesia lagoon managers are currently establishing zoning plans of pearl farming lagoons that typically reserve areas to rear stocks, and areas to collect spats.

Nevertheless, lagoon hydrodynamics and connectivity modeling studies (Dumas et al., 2012; Thomas et al., 2012, 2014, 2016) can help understanding sink areas for *Pinctada margaritifera* larvae for a given regime and therefore the most suitable areas for spat collection in a 'regime' condition.

Other relevant products would be to use atoll hydrodynamic and dispersal models forced by the different wind regimes, to estimate where would be the best 'source' areas to maximize reproduction and spat collection. This time, instead of identifying sinks for spat collection as described just above, the objectives would be to identify the best sources of larvae to target spat collecting in existing concessions, and, for instance, replenish natural stocks in these source areas to maximize the reproduction success. All these applications on stock management, or spatial planning, will benefit from model outputs computed in all regime conditions weighted by their frequency of occurrence, thus representing a number of recurrent conditions throughout the year with a known frequency.

Finally, Andréfouët et al. (2015) previously investigated the environmental conditions that could explain massive benthic mortalities in Tuamotu and Cook Islands atoll lagoons. These events remain a constant threat for the pearl famring industry, and the most recent case occurred in 2013-2014 in Takaroa atoll, where all the activity was stopped abruptly after that an algal bloom impacted directly the resources (Rodier et al; 2019). As in 2020, the farming activity has not yet recovered in Takaroa. A conclusion from Andréfouët et al. (2015) was that mortality could impact very selectively some atolls but not others due to the spatial scale of distribution of the calm, environmental conditions that trigger mortalities. The results of the present study confirm that atolls are not equal in term of their wind regimes, even if there are a low number of regimes overall. The relationships between regimes, their occurrences, and the occurrence of calm periods necessary to trigger mortalities warrant further investigations.

To the best of our knowledge, these applications will be the first case of resource management in South Pacific Islands that would be constrained by appropriate knowledge and characterization of wind regimes, at present time and in the future. It is anticipated that such tools will be tested and implemented in a short future in French Polynesia.

Acknowledgements

This study was funded by grant ANR-16-CE32-0004 MANA (Management of Atolls project). The authors acknowledge the Pôle de Calcul et de Données Marines (PCDM) for providing DATARMOR storage and computational resources (http://www.ifremer.fr/pcdm).

References

Andréfouët, S., Charpy, L., Lo-Yat, A., and Lo, C. (2012). Recent research for pearl oyster aquaculture management in French Polynesia. Marine Pollution Bulletin *65*, 407–414.

Andréfouët, S., Dutheil, C., Menkes, C.E., Bador, M., and Lengaigne, M. (2015). Mass mortality events in atoll lagoons: environmental control and increased future vulnerability. Global Change Biology *21*, 195–205.

Brown, J.N., Langlais, C., and Sen Gupta, A. (2015). Projected sea surface temperature changes in the equatorial Pacific relative to the Warm Pool edge. Deep Sea Research Part II: Topical Studies in Oceanography *113*, 47–58.

Brown, J.R., Lengaigne, M., Benjamin R. Lintner, Widlansky, M.J., van der Wiel, K., Dutheil, C., Linsley, B.K., Matthews, A.J., and Renwick, J. (2020). South Pacific Convergence Zone dynamics, variability, and impacts in a changing climate. Nature Reviews Earth and Environment, *accepted*.

Cai, W., Lengaigne, M., Borlace, S., Collins, M., Cowan, T., McPhaden, M.J., Timmermann, A., Power, S., Brown, J., Menkes, C., et al., (2012). More extreme swings of the South Pacific convergence zone due to greenhouse warming. Nature *488*, 365–369.

Cai, W., Borlace, S., Lengaigne, M., van Rensch, P., Collins, M., Vecchi, G., Timmermann, A., Santoso, A., McPhaden, M.J., Wu, L., et al., (2014). Increasing frequency of extreme El Niño events due to greenhouse warming. Nature Climate Change *4*, 111–116.

Cai, W., Wang, G., Dewitte, B., Wu, L., Santoso, A., Takahashi, K., Yang, Y., Carréric, A., and McPhaden, M.J. (2018). Increased variability of eastern Pacific El Niño under greenhouse warming. Nature *564*, 201–206.

Charrad, M., Ghazzali, N., Boiteau, V., and Niknafs, A. (2014). NbClust : An R Package for Determining the Relevant Number of Clusters in a Data Set. J. Stat. Soft. *61*.

Chung, C.T.Y., and Power, S.B. (2016). Modelled impact of global warming on ENSO-driven precipitation changes in the tropical Pacific. Climate Dynamics *47*, 1303–1323.

Claar, D.C., Szostek, L., McDevitt-Irwin, J.M., Schanze, J.J., Baum, J.K., 2018. Global patterns and impacts of El Niño events on coral reefs: A meta-analysis. PLoS ONE 13, e0190957.

Collins, M., An, S.-I., Cai, W., Ganachaud, A., Guilyardi, E., Jin, F.-F., Jochum, M., Lengaigne, M., Power, S., Timmermann, A., et al., (2010). The impact of global warming on the tropical Pacific Ocean and El Niño. Nature Geoscience *3*, 391–397.

Cuif, M., Kaplan, D.M., Lefèvre, J., Faure, V.M., Caillaud, M., Verley, P., Vigliola, L., and Lett, C. (2014). Wind-induced variability in larval retention in a coral reef system: A biophysical modelling study in the South-West Lagoon of New Caledonia. Progress in Oceanography *122*, 105–115.

Dumas, F., Le Gendre, R., Thomas, Y., and Andréfouët, S. (2012). Tidal flushing and wind driven circulation of Ahe atoll lagoon (Tuamotu Archipelago, French Polynesia) from in situ observations and numerical modelling. Marine Pollution Bulletin *65*, 425–440.

Dutheil, C., Bador M., Lengaigne M., Lefèvre J., Jourdain N. C., Vialard J., Jullien Swen, Peltier A., Menkes C. (2019). Impact of surface temperature biases on climate change projections of the South Pacific Convergence Zone . Climate Dynamics , 53(5-6), 3197-3219. https://doi.org/10.1007/s00382-019-04692-6

Dutheil, C., Lengaigne, M., Bador, M. et al. Impact of projected sea surface temperature biases on tropical cyclones projections in the South Pacific. Scientific Reports 10, 4838 (2020). https://doi.org/10.1038/s41598-020-61570-6

E. Diday (1971). Une nouvelle méthode en classification automatique et reconnaissance des formes la méthode des nuées dynamiques. Revue de Statistique Appliquée 19–33.

Evans, J.P., Bormann, K., Katzfey, J., Dean, S., and Arritt, R. (2016). Regional climate model projections of the South Pacific Convergence Zone. Climate Dynamics *47*, 817–829.

Folland, C.K. (2002). Relative influences of the Interdecadal Pacific Oscillation and ENSO on the South Pacific Convergence Zone. Geophysical Research Letters *29*, 211–214.

Fournier, J., Levesque, E., Pouvreau, S., Pennec, M.L., and Moullac, G.L. (2012). Influence of plankton concentration on gametogenesis and spawning of the black lip pearl oyster Pinctada margaritifera in Ahe atoll lagoon (Tuamotu archipelago, French polynesia). Marine Pollution Bulletin *65*, 463–470.

Gastineau, G., Treut, H.L., and Li, L. (2008). Hadley circulation changes under global warming conditions indicated by coupled climate models. Tellus A: Dynamic Meteorology and Oceanography *60*, 863–884.

Grose, M.R., Brown, J.N., Narsey, S., Brown, J.R., Murphy, B.F., Langlais, C., Gupta, A.S., Moise, A.F., and Irving, D.B. (2014). Assessment of the CMIP5 global climate model simulations of the western tropical Pacific climate system and comparison to CMIP3: assesment of CMIP5 climate models for the western tropical pacific. International Journal of Climatology *34*, 3382–3399.

Harvell, C.D., 2002. Climate Warming and Disease Risks for Terrestrial and Marine Biota. Science 296, 2158–2162.

Hopuare, M., Guglielmino, M., and Ortega, P. (2019). Interactions between intraseasonal and diurnal variability of precipitation in the South Central Pacific: The case of a small high island, Tahiti, French Polynesia. Int J Climatol *39*, 670–686.

Jolliffe, I. (2011). Principal Component Analysis. In International Encyclopedia of Statistical Science, M. Lovric, ed. (Berlin, Heidelberg: Springer Berlin Heidelberg), pp. 1094–1096.

Kanamitsu, M., Ebisuzaki, W., Woollen, J., Yang, S.-K., Hnilo, J.J., Fiorino, M., and Potter, G.L. (2002). NCEP–DOE AMIP-II Reanalysis (R-2). Bulletin of the American Meteorological Society *83*, 1631–1643.

Kiladis, G.N., von Storch, H., and Loon, H. (1989). Origin of the South Pacific Convergence Zone. Journal of Climate *2*, 1185–1195.

Lefèvre, J., Marchesiello, P., Jourdain, N.C., Menkes, C., and Leroy, A. (2010). Weather regimes and orographic circulation around New Caledonia. Marine Pollution Bulletin *61*, 413–431.

Leroy, A. (2006). Utilisation des Prévisions Saisonnières en Nouvelle-Calédonie. Note de la DP n° 6, Météo-France, DP/DCLIM.

Li, G., Du, Y., Xu, H., and Ren, B. (2015). An Intermodel Approach to Identify the Source of Excessive Equatorial Pacific Cold Tongue in CMIP5 Models and Uncertainty in Observational Datasets. Journal of Climate *28*, 7630–7640.

Li, G., Xie, S.-P., Du, Y., and Luo, Y. (2016). Effects of excessive equatorial cold tongue bias on the projections of tropical Pacific climate change. Part I: the warming pattern in CMIP5 multi-model ensemble. Climate Dynamics *47*, 3817–3831.

Lorrey, A.M., and Fauchereau, N.C. (2018). Southwest Pacific atmospheric weather regimes: linkages to ENSO and extra-tropical teleconnections: Southwest Pacific atmospheric weather regimes: linkages to ENSO and extra-tropical teleconnections. Int. J. Climatol *38*, 1893–1909.

Lowe, R.J., and Falter, J.L. (2015). Oceanic Forcing of Coral Reefs. Annual Review of Marine Science *7*, 43–66.

Rodier, M., Longo, S., Henry, K., Ung, A., Lo-Yat, A., Darius, H., Viallon, J., Beker, B., Delesalle, B., Chinain, M., 2019. Diversity and toxic potential of algal bloom-forming species from Takaroa lagoon (Tuamotu, French Polynesia): a field and mesocosm study. Aquat. Microb. Ecol. 83, 15–34. https://doi.org/10.3354/ame01900

Salinger, M.J., Renwick, J.A., and Mullan, A.B. (2001). Interdecadal Pacific Oscillation and South Pacific climate. Int. J. Climatol. *21*, 1705–1721.

Skamarock, W.C., and Klemp, J.B. (2008). A time-split nonhydrostatic atmospheric model for weather research and forecasting applications. Journal of Computational Physics *227*, 3465–3485.

Specq, D., Bellon, G., Peltier, A., Lefévre, J., and Menkes, C. (2019). Influence of subseasonal variability on the diurnal cycle of precipitation on a mountainous island: the case of New Caledonia. Mon. Wea. Rev. MWR-D-19-0177.1.

Thomas, Y., Garen, P., Courties, C., Charpy, L., 2010. Spatial and temporal variability of the pico- and nanophytoplankton and bacterioplankton in a deep Polynesian atoll lagoon. Aquatic Microbial Ecology 59, 89–101.

Thomas, Y., Le Gendre, R., Garen, P., Dumas, F., and Andréfouët, S. (2012). Bivalve larvae transport and connectivity within the Ahe atoll lagoon (Tuamotu Archipelago), with application to pearl oyster aquaculture management. Marine Pollution Bulletin *65*, 441–452.

Thomas, Y., Dumas, F., and Andréfouët, S. (2014). Larval Dispersal Modeling of Pearl Oyster *Pinctada margaritifera* following Realistic Environmental and Biological Forcing in Ahe Atoll Lagoon. PLoS ONE *9*, e95050.

Thomas, Y., Dumas, F., and Andréfouët, S. (2016). Larval connectivity of pearl oyster through biophysical modelling; evidence of food limitation and broodstock effect. Estuarine, Coastal and Shelf Science *182*, 283–293.

Timmermann, A., An, S.-I., Kug, J.-S., Jin, F.-F., Cai, W., Capotondi, A., Cobb, K., Lengaigne, M., McPhaden, M.J., Stuecker, M.F., et al., (2018). El Niño–Southern Oscillation complexity. Nature *559*, 535–545.

Tokinaga, H., Xie, S.-P., Deser, C., Kosaka, Y., and Okumura, Y.M. (2012). Slowdown of the Walker circulation driven by tropical Indo-Pacific warming. Nature *491*, 439–443.

Van Wynsberge, S., Menkes, C., Le Gendre, R., Passfield, T., and Andréfouët, S. (2017a). Are Sea Surface Temperature satellite measurements reliable proxies of lagoon temperature in the South Pacific? Estuarine, Coastal and Shelf Science *199*, 117–124.

Van Wynsberge, S., Andréfouët, S., Gaertner-Mazouni, N., Wabnitz, C.C.C., Menoud, M., Le Moullac, G., Levy, P., Gilbert, A., and Remoissenet, G. (2017b). Growth, Survival and Reproduction of the Giant Clam Tridacna maxima (Röding 1798, Bivalvia) in Two Contrasting Lagoons in French Polynesia. PLoS ONE *12*, e0170565.

Vecchi, G.A., Soden, B.J., Wittenberg, A.T., Held, I.M., Leetmaa, A., and Harrison, M.J. (2006). Weakening of tropical Pacific atmospheric circulation due to anthropogenic forcing. Nature *441*, 73–76.

Vecchi, G.A., Clement, A., and Soden, B.J. (2008). Examining the tropical Pacific's response to global warming. Eos, Transactions American Geophysical Union *89*, 81–83.

Vincent, D.G. (1994). The South Pacific Convergence Zone (SPCZ): A Review. Monthly Weather Review *122*, 1949–1970.

Vincent, E.M., Lengaigne, M., Menkes, C.E., Jourdain, N.C., Marchesiello, P., and Madec, G. (2011). Interannual variability of the South Pacific Convergence Zone and implications for tropical cyclone genesis. Climate Dynamics *36*, 1881–1896.

Widlansky, M.J., Timmermann, A., Stein, K., McGregor, S., Schneider, N., England, M.H., Lengaigne, M., and Cai, W. (2013). Changes in South Pacific rainfall bands in a warming climate. Nature Climate Change *3*, 417–423.

van der Wiel, K., Matthews, A.J., Joshi, M.M., and Stevens, D.P. (2016). Why the South Pacific Convergence Zone is diagonal., Climate Dynamics *46*, 1683–1698.

Xie, P., and Arkin, P.A. (1997). Global Precipitation: A 17-Year Monthly Analysis Based on Gauge Observations, Satellite Estimates, and Numerical Model Outputs. Bulletin of the American Meteorological Society *78*, 2539–2558.

Zhang, C., Wang, Y., Hamilton, K., and Lauer, A. (2016). Dynamical Downscaling of the Climate for the Hawaiian Islands. Part II: Projection for the Late Twenty-First Century. Journal of Climate *29*, 8333–8354.

Figure 1: (a) Map representing the domain where the weather regimes are computed. The archipelagos studied here are surrounded by different colors, and the pearl farming sites selected are indicated. (b) Annual mean climatologies of precipitation from CMAP (shading; in mm.day-1), mean sea level pressure (contours; in hPa) and surface winds (vectors, in m.s-1) from NCEP2 reanalysis. The entire displayed domain (d01) represents the parent domain of WRF simulations, the d02 domain (black box) represents the child domain of WRF simulations, and the “WR domain” (blue box) represents the domain where the weather regime were calculated. The letters “H” and “L” indicated the mean position of South Pacific High and equatorial low pressure zone, respectively. The pink contour displays the 5mm.day-1 average rainfall in south Pacific indicating the SPCZ limits.

Figure 2: Top: (a) Multi-model mean (MMM) CMIP5 of precipitation bias (in mm.day^{-1}) relative to observations (CMAP). (b) Relationships between the SST projected changes (°C) and the historical mean precipitation (mm.day^{-1}) in the equatorial western Pacific (160°E-170°W;2°S-2°N) among 31 CMIP5 models (red dots). The inter-model correlation (r) is shown at the bottom-left. The dashed lines on the panels b denote the observed mean precipitation in the equatorial western Pacific.
Bottom: DJF climatology (shading, in °C) of (e) ΔSST_{CMIP} and (f) ΔSST_{COR}. ΔSST_{CMIP} and ΔSST_{COR} are respectively the uncorrected and the corrected projected SST pattern. The contours represent the DJF climatology of precipitation (in mm.d^{-1}) changes between (e) CC and PD, (f)

COR and PD simulations. The dashed lines indicate negative values, while the thick lines indicates positive values.

Figure 3: Distribution of the number of clusters for all indicators included in NbClust for (a) daily WRs and (b) 30-day WRs.

Figure 4: Surface winds (shading and vectors, in m.s^{-1}) composite maps showing the four weather regimes over the 37-years period from (1st row) the ERA-5 reanalysis, (2nd row) PD simulation, (3rd row) and (4th row) changes between CC and PD.

Figure 5: (a) Percentage of days of each weather regime included in homogeneous spells lasting at least 3, 6, 9 and 12 days; (b) Monthly mean occurrence of weather types.

Figure 6: Surface winds (vectors, in m.s^{-1}), surface pressure (contours, in hPa) and precipitation (shading, in mm.day^{-1}) composite maps showing the four weather regimes 37-years period from (1st row) PD, (2nd row) CC, and (3rd row) changes between CC and PD. The blue box shows the domain on which the weather regimes were calculated (Fig. 1). The pink contours show the isoline 6mm.day^{-1} representing SPCZ limits.

Figure 7: Surface wind anomalies (in m.s^{-1}) in PD for each weather regime (first row) and each ENSO phase (second row). The anomalies are computed in relation to the period-average.

Figure 8: Surface wind speed (left; in m.s^{-1}), and direction (right; in °N) for the barycenter of each nine 30-day weather regimes over 1980-2016 period from the PD simulation. The right-hand boxes show the colors to identify each regime, and the occurrence frequency (in %) is indicated.

Figure 9: Surface wind (shading and vectors, in m.s^{-1}) composite maps showing the barycenter of S1, 2 and 5 from PD simulation. The 30-day sequences are split in five 6-days sequences. Each panel represents the time average of a 6-day sequence.

Figure 10: Surface wind speed (left; in $m.s^{-1}$), and direction (right; in °N) for S1, 2 and 5 for the period 1980-2016 from the PD simulation. The right-hand boxes show the colors that identify each regime.

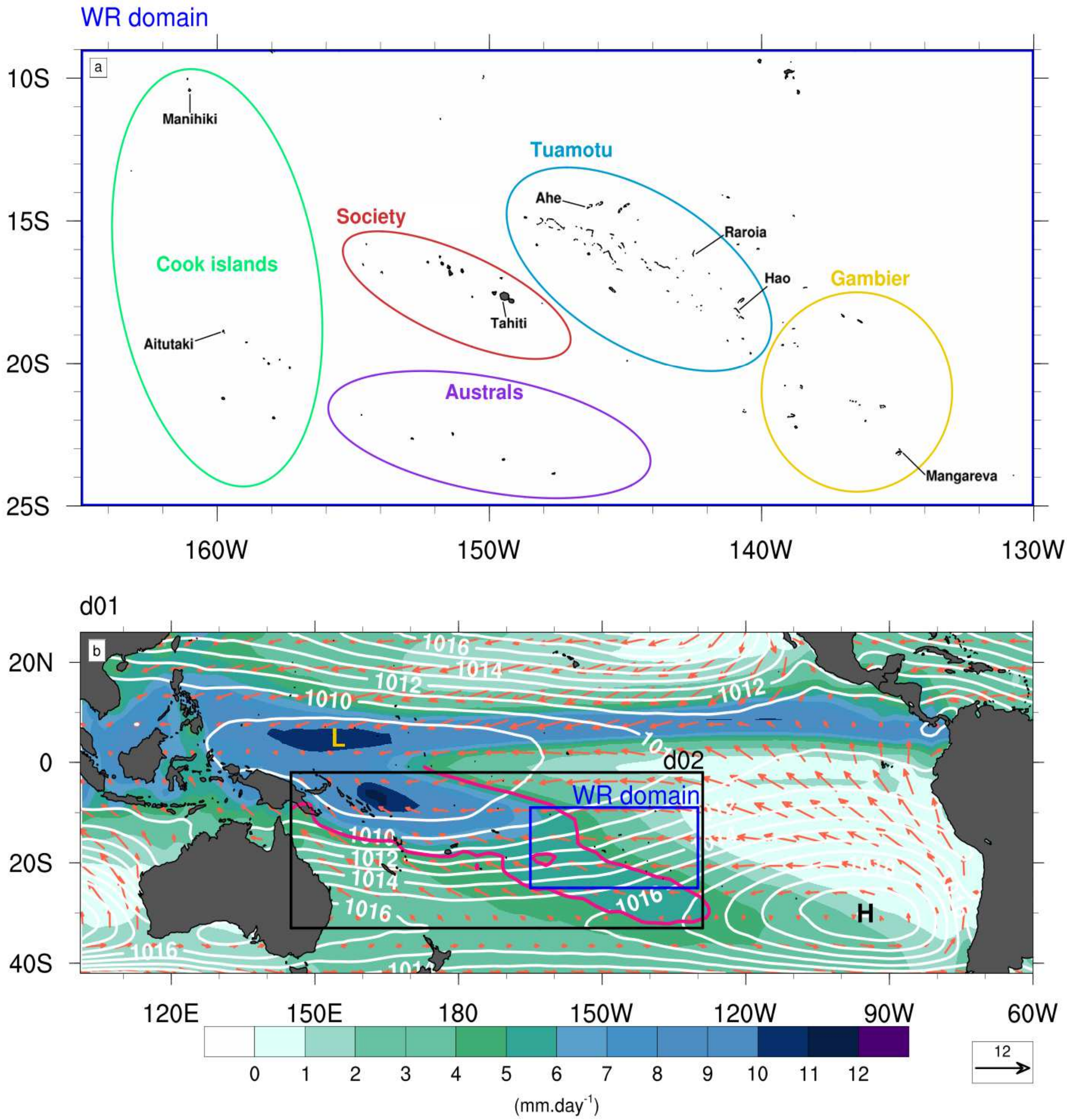
WR domain
a
Manihiki
Cook islands
Aitutaki
Society
Tahiti
Australs
Tuamotu
Ahe
Raroia
Hao
Gambier
Mangareva
10S
15S
20S
25S
160W
150W
140W
130W
d01
b
d02
WR domain
L
H
1010
1012
1014
1016
20N
0
20S
40S
120E
150E
180
150W
120W
90W
60W
0
1
2
3
4
5
6
7
8
9
10
11
12
(mm.day-1)
12

769 **Figure 1**

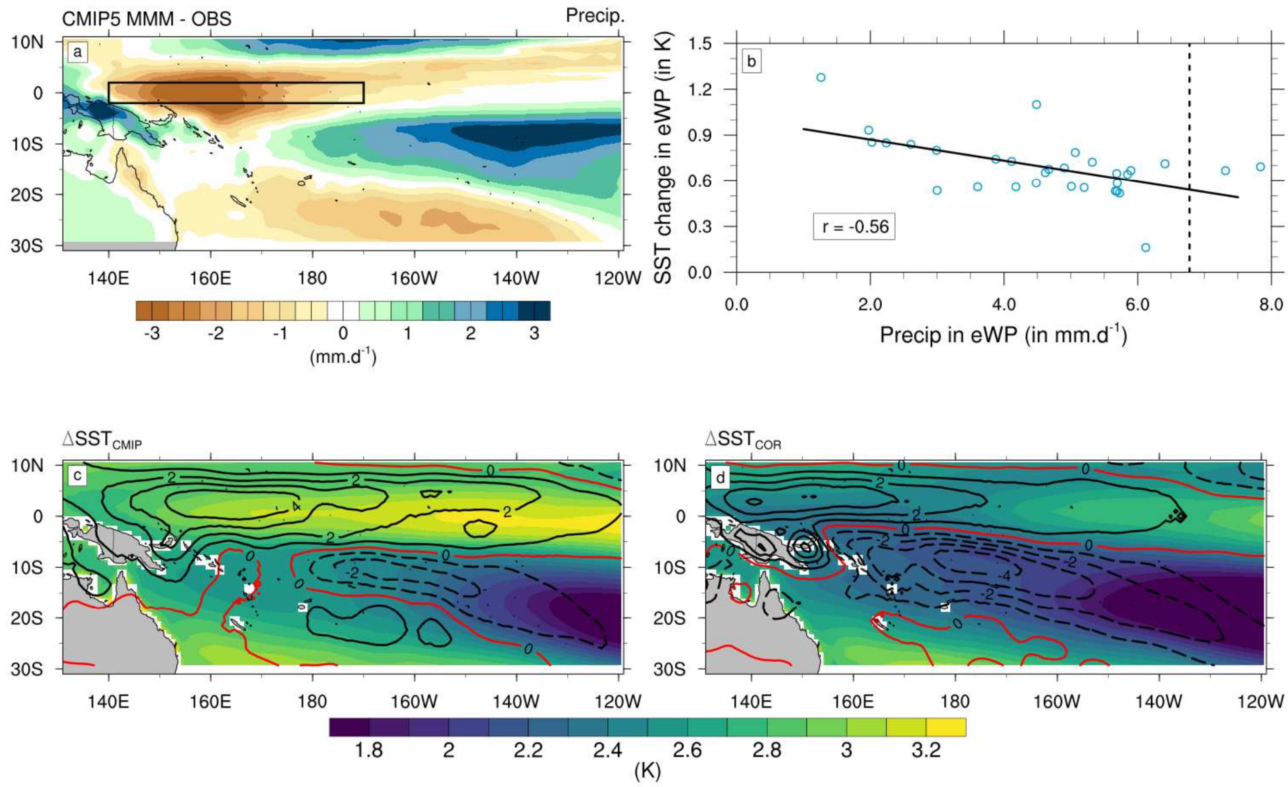
CMIP5 MMM - OBS
Precip.
a
10N
0
10S
20S
30S
140E
160E
180
160W
140W
120W
-3
-2
-1
0
1
2
3
(mm.d-1)
b
SST change in eWP (in K)
1.5
1.2
0.9
0.6
0.3
0.0
r = -0.56
0.0
2.0
4.0
6.0
8.0
Precip in eWP (in mm.d-1)
ΔSST_CMIP
c
ΔSST_COR
d
1.8
2
2.2
2.4
2.6
2.8
3
3.2
(K)

770 **Figure 2**

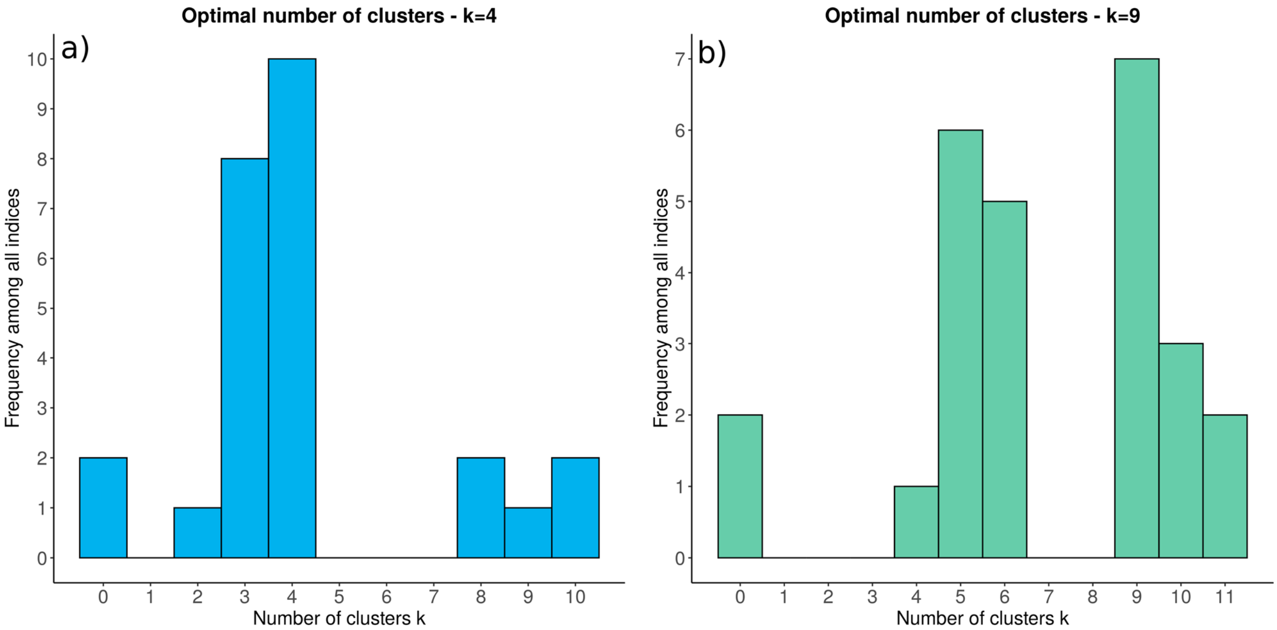
Optimal number of clusters - k=4
a)
Frequency among all indices
Number of clusters k
Optimal number of clusters - k=9
b)
Frequency among all indices
Number of clusters k

Figure 3

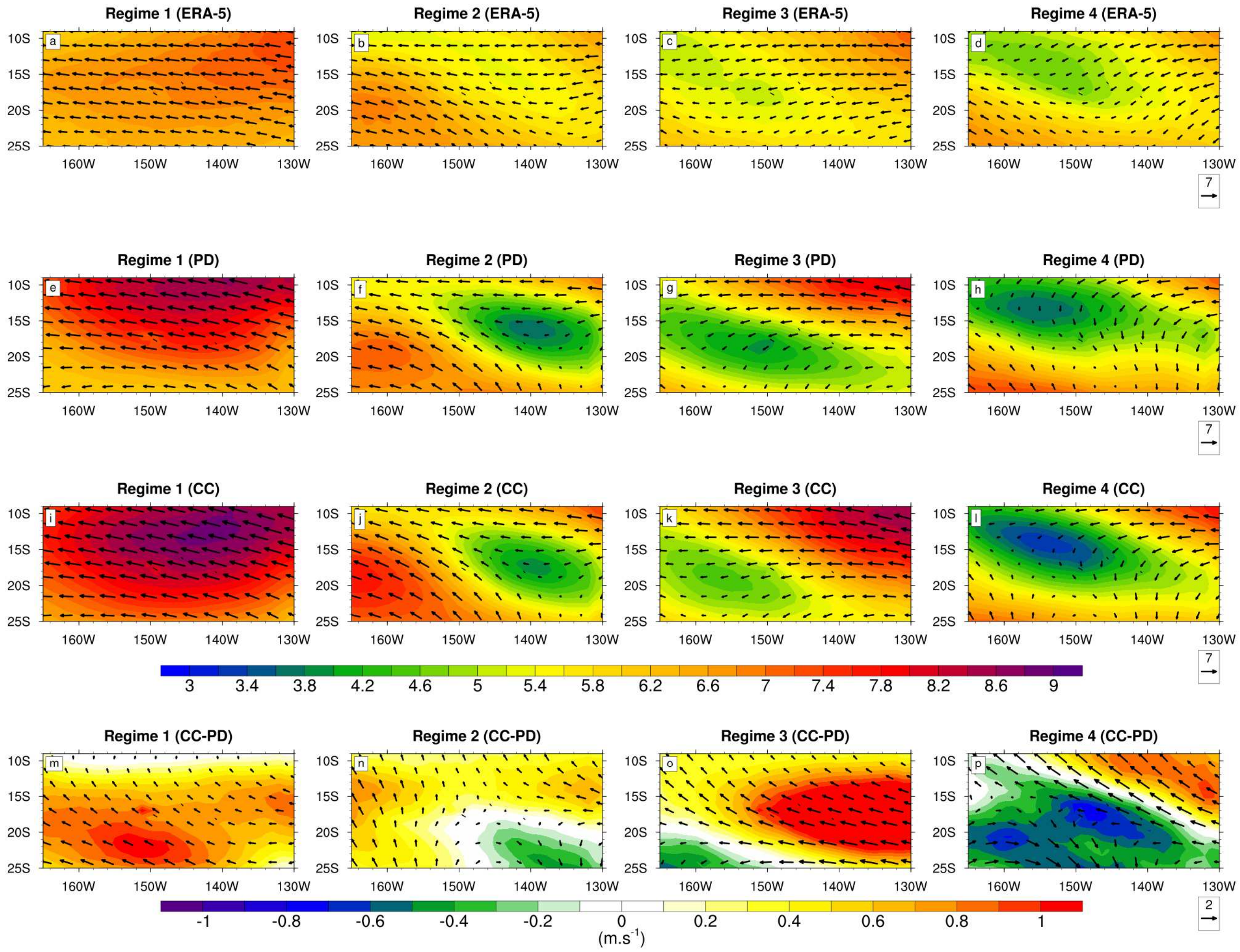
Regime 1 (ERA-5)
Regime 2 (ERA-5)
Regime 3 (ERA-5)
Regime 4 (ERA-5)
Regime 1 (PD)
Regime 2 (PD)
Regime 3 (PD)
Regime 4 (PD)
Regime 1 (CC)
Regime 2 (CC)
Regime 3 (CC)
Regime 4 (CC)
Regime 1 (CC-PD)
Regime 2 (CC-PD)
Regime 3 (CC-PD)
Regime 4 (CC-PD)
10S
15S
20S
25S
160W
150W
140W
130W
3
3.4
3.8
4.2
4.6
5
5.4
5.8
6.2
6.6
7
7.4
7.8
8.2
8.6
9
-1
-0.8
-0.6
-0.4
-0.2
0
0.2
0.4
0.6
0.8
1
(m.s-1)

772

Figure 4

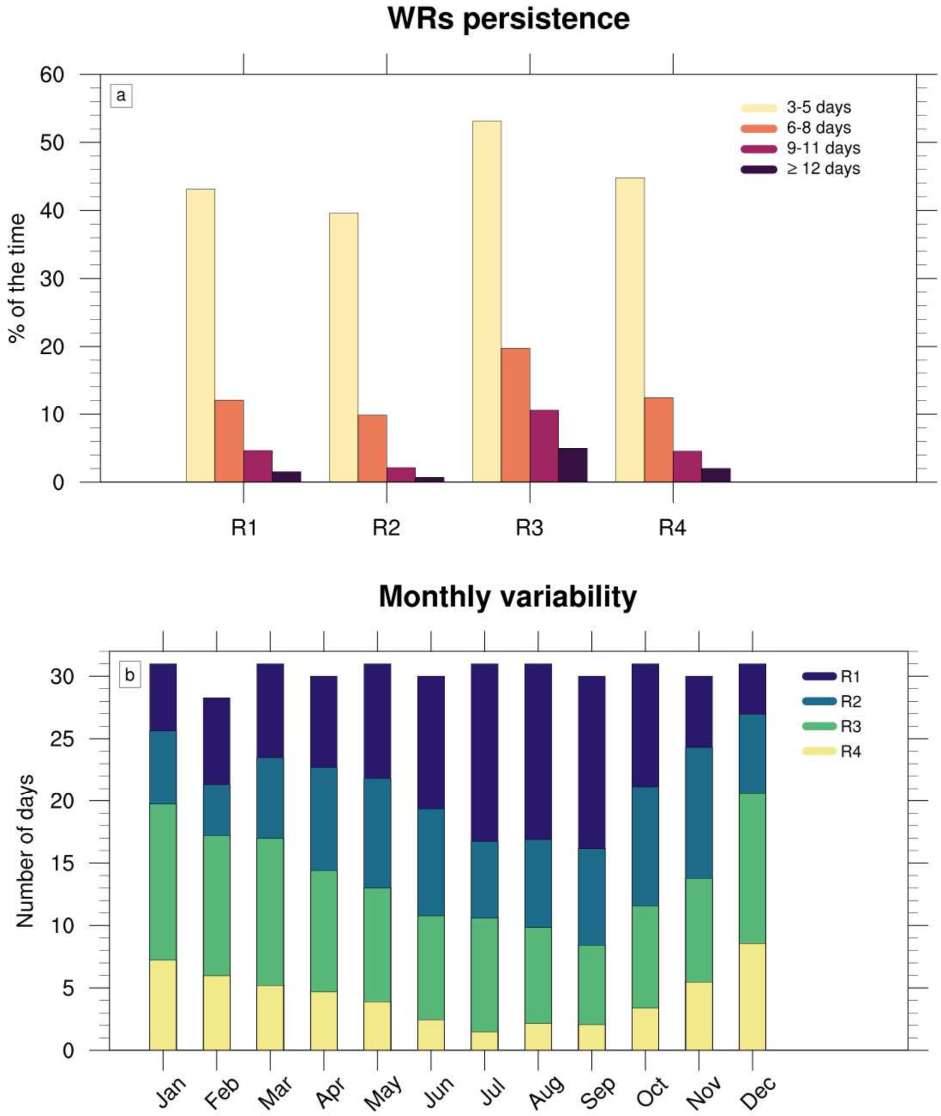
WRs persistence
a
3-5 days
6-8 days
9-11 days
≥ 12 days
% of the time
0
10
20
30
40
50
60
R1
R2
R3
R4
Monthly variability
b
R1
R2
R3
R4
Number of days
0
5
10
15
20
25
30
Jan
Feb
Mar
Apr
May
Jun
Jul
Aug
Sep
Oct
Nov
Dec

773 **Figure 5**

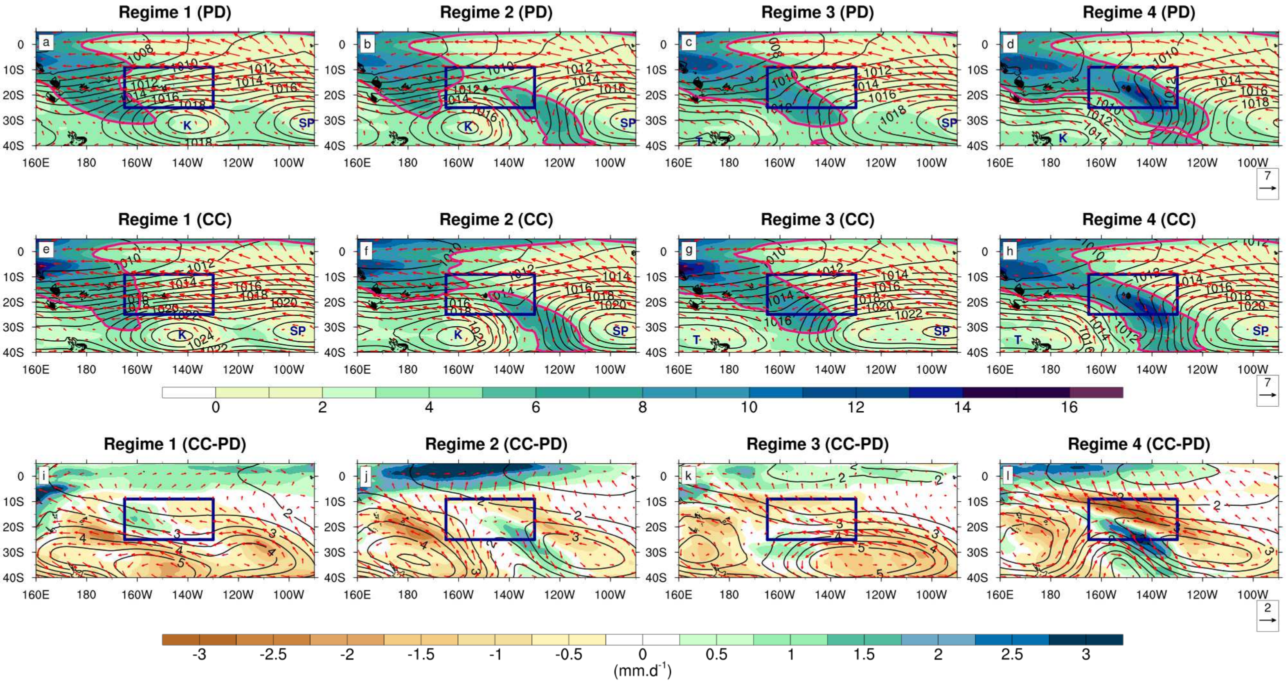

Regime 1 (PD)
Regime 2 (PD)
Regime 3 (PD)
Regime 4 (PD)
Regime 1 (CC)
Regime 2 (CC)
Regime 3 (CC)
Regime 4 (CC)
Regime 1 (CC-PD)
Regime 2 (CC-PD)
Regime 3 (CC-PD)
Regime 4 (CC-PD)
(mm.d-1)

774

Figure 6

775

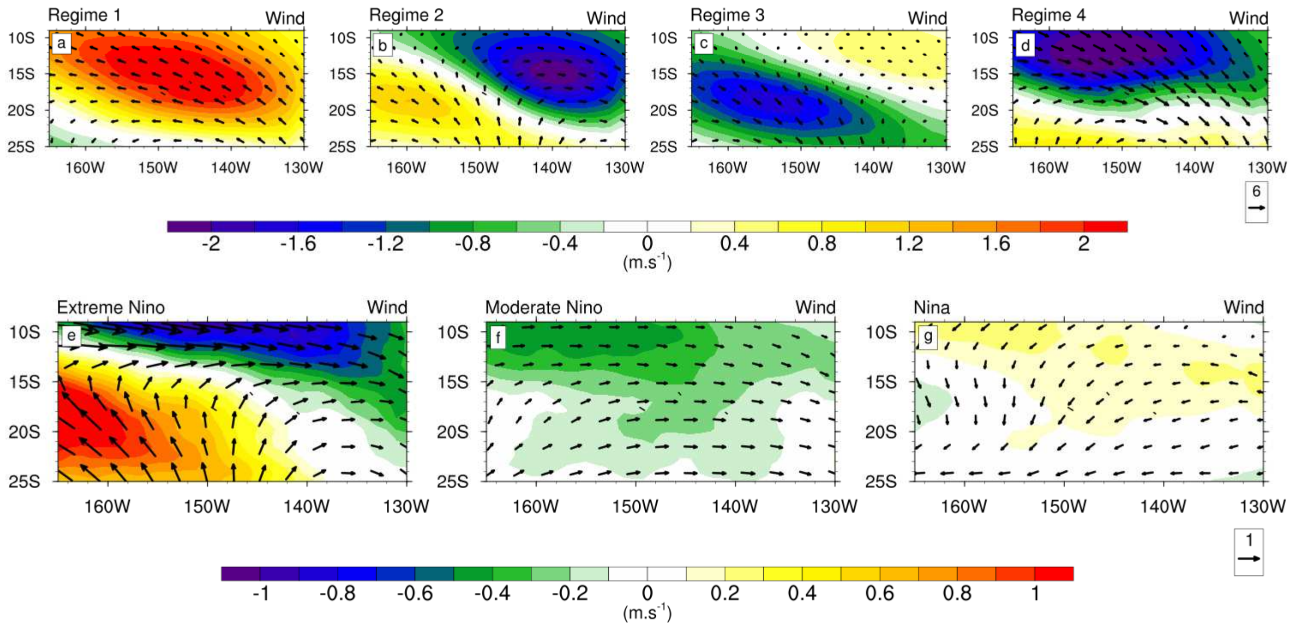

Regime 1
Wind
a
Regime 2
Wind
b
Regime 3
Wind
c
Regime 4
Wind
d
10S
15S
20S
25S
160W
150W
140W
130W
6
-2
-1.6
-1.2
-0.8
-0.4
0
0.4
0.8
1.2
1.6
2
(m.s-1)
Extreme Nino
Wind
e
Moderate Nino
Wind
f
Nina
Wind
g
1
-1
-0.8
-0.6
-0.4
-0.2
0
0.2
0.4
0.6
0.8
1
(m.s-1)

Figure 7

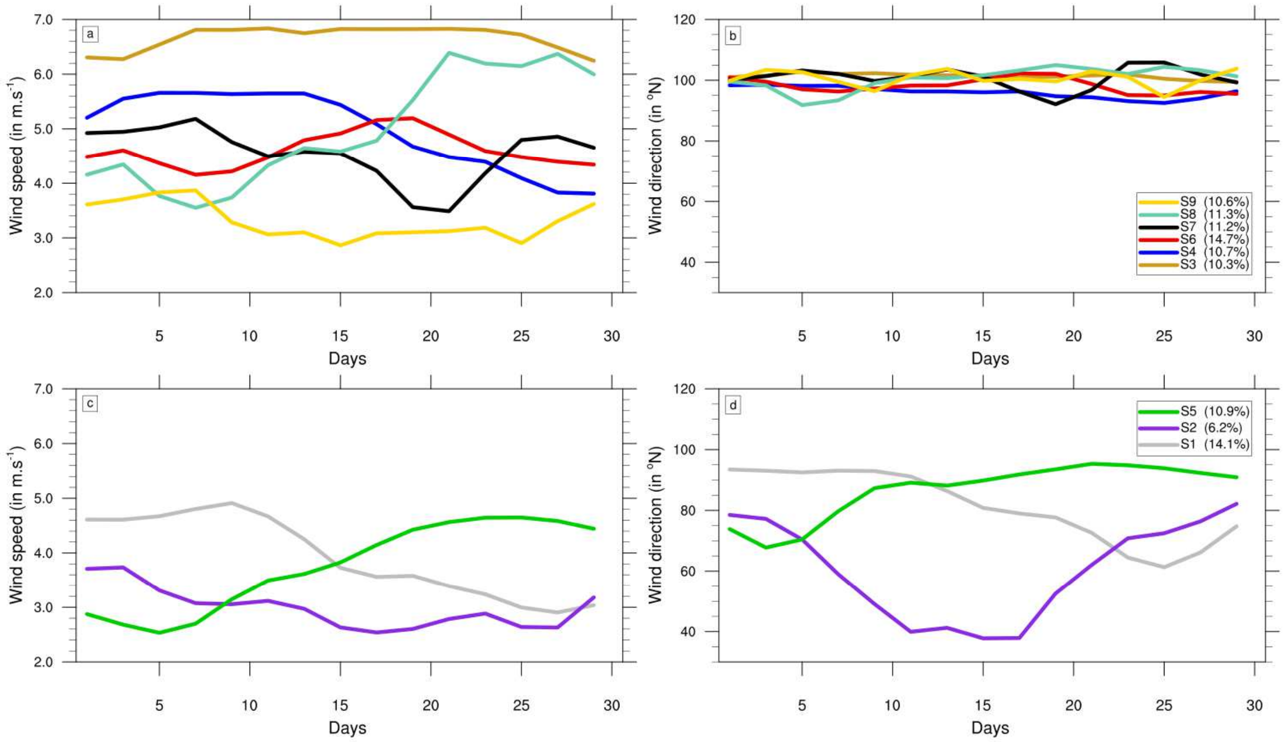
a
b
c
d
Wind speed (in m.s-1)
Wind direction (in °N)
Days
S9 (10.6%)
S8 (11.3%)
S7 (11.2%)
S6 (14.7%)
S4 (10.7%)
S3 (10.3%)
S5 (10.9%)
S2 (6.2%)
S1 (14.1%)

776 **Figure 8**

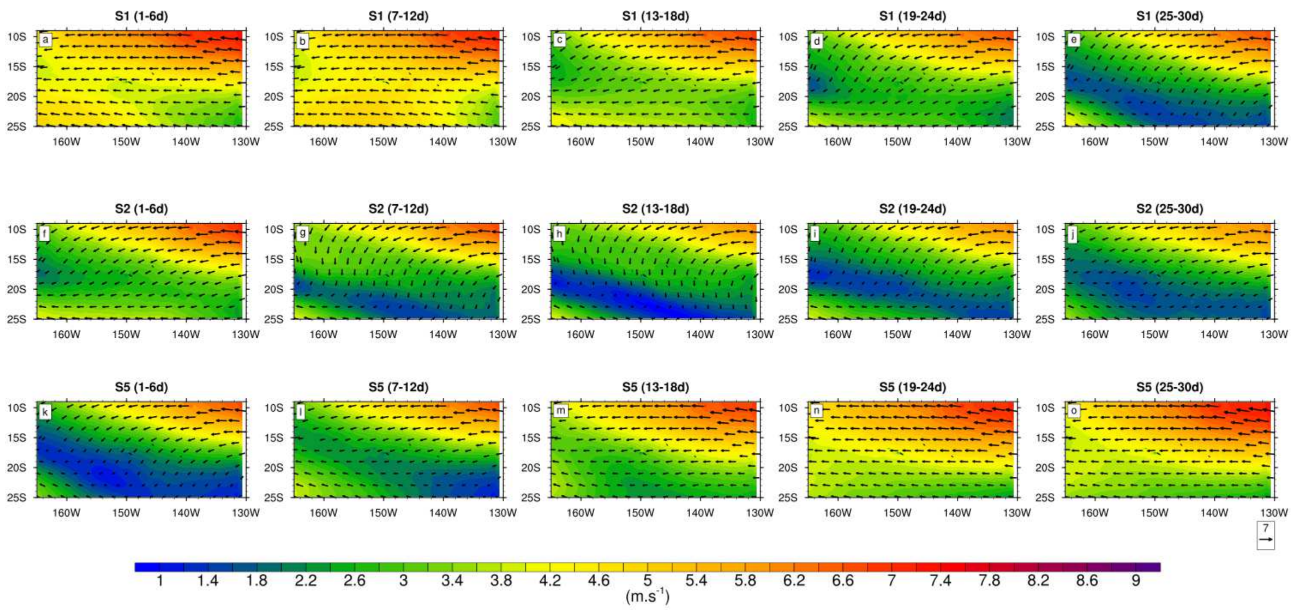

S1 (1-6d)
S1 (7-12d)
S1 (13-18d)
S1 (19-24d)
S1 (25-30d)
S2 (1-6d)
S2 (7-12d)
S2 (13-18d)
S2 (19-24d)
S2 (25-30d)
S5 (1-6d)
S5 (7-12d)
S5 (13-18d)
S5 (19-24d)
S5 (25-30d)
a
b
c
d
e
f
g
h
i
j
k
l
m
n
o
10S
15S
20S
25S
160W
150W
140W
130W
7
1
1.4
1.8
2.2
2.6
3
3.4
3.8
4.2
4.6
5
5.4
5.8
6.2
6.6
7
7.4
7.8
8.2
8.6
9
(m.s-1)

777 **Figure 9**

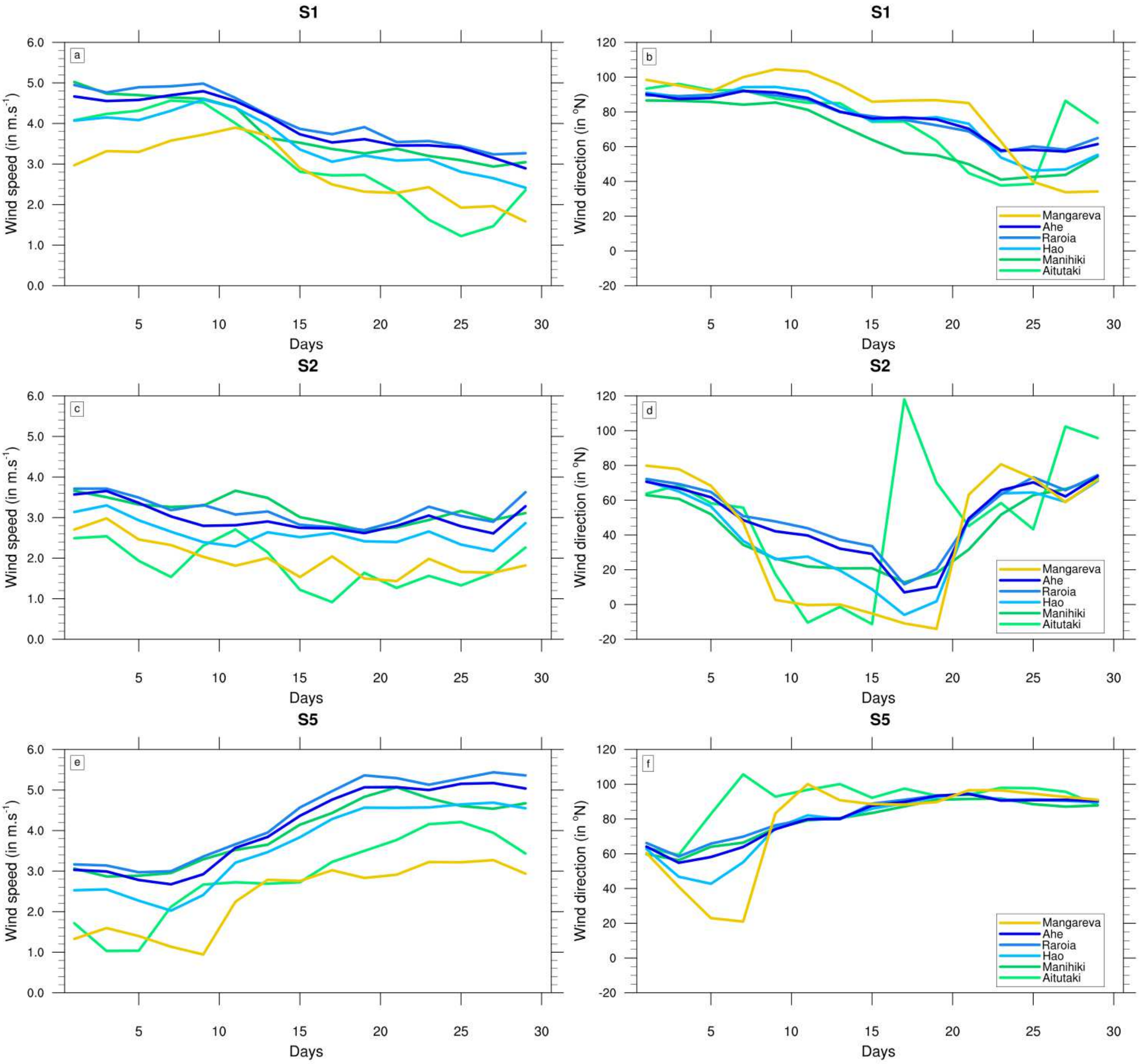

S1
a
Wind speed (in m.s^{-1})
Days
b
Wind direction (in °N)
Mangareva
Ahe
Raroia
Hao
Manihiki
Aitutaki
S2
c
d
S5
e
f

Figure 10

Table 1: Statistics of wind composite parameters (speed and direction in average) computed from ERA5 reanalysis, and the PD and CC simulations over 37-years period (1980-2016 for ERA5 and PD; and 2072-2108 for CC).

	Frequency			Wind speed (in $m.s^{-1}$)			Wind direction (°N)		
	ERA5	PD	CC	ERA5	PD	CC	ERA5	PD	CC
R1	4559 (34.3%)	3944 (29.7%)	3936 (29.7%)	6.3	6.8	7.6	99.3	102.1	104.8
R2	3042 (22.9%)	3250 (24.5%)	2670 (20.1%)	4.4	4.2	4.5	107.5	109.2	113.0
R3	3846 (29.0%)	4164 (31.4%)	4640 (35.0%)	3.9	4.0	5.2	75.3	84.7	91.3
R4	1823 (13.7%)	1912 (14.4%)	2024 (15.3%)	3.0	2.7	3.1	64.9	61.0	73.1

Table 2: Results of the goodness-of-fit test between observed and expected days, assuming that the distribution of the weather type does not depend on ENSO phases. O: Observed; E: Expected; R: standardized residual. Absolute values of R greater than 2 are in bold; positive (negative) values indicate that regime is likely (unlikely) to occur during the corresponding phase.

		R1	R2	R3	R4
Extreme El Niño	O	251	354	227	205
	E	308	254	325	149
	R	**-3.3**	**6.3**	**-5.4**	**4.6**
Moderate El Niño	O	681	754	827	472
	E	813	670	858	394
	R	**-4.6**	**3.2**	-1.1	**3.9**
Neutral	O	1840	1437	1881	720
	E	1747	1440	1844	847
	R	**2.1**	-0.08	0.9	**-4.7**
La Niña	O	1172	705	1229	515
	E	1076	887	1136	522
	R	**2.9**	**-6.1**	**2.8**	-0.3
Chi-square	p-value	<0.001	<0.001	<0.001	<0.001

Table 3 : Spatial pattern correlation of surface wind composites anomalies between each daily weather regime and ENSO mode. The anomalies are calculated from the average over the 1980-2016 period. Absolute spatial pattern correlation values greater than 0.6 are in bold.

	R1	R2	R3	R4
Extreme El Niño	-0.51	**0.88**	**-0.86**	0.58
Moderate El Niño	**-0.63**	0.40	-0.34	**0.80**
La Niña	**0.61**	**-0.66**	0.55	**-0.64**

Table 4 : Typology on wind direction of nine 30-day regimes.

Easterly steady direction	East + North-north-east	East + North-east	North-east + East
S3, 4, 6, 7, 8 and 9	S2	S1	S5